PHOTONIC SENSORS / Vol. 16, No. 3, 2026: 9560021

Self-Assembled 10 nm-Nanogap Arrays With High-Density Hot Spot Distribution for Environmental Pollutant Detection

Zhiliang ZHANG[1,2†], Peibin XU[3†], Hao WU[1,2], Churong MA[1,2], Jiahao YAN[2,4], Tuan GUO[1,2], Dali WANG[3*], and Kai CHEN[1,2*]

[1]*Guangdong Provincial Key Laboratory of Optical Fiber Sensing and Communications, Institute of Photonics Technology, Jinan University, Guangzhou 511443, China*

[2]*College of Physics and Optoelectronic Engineering, Jinan University, Guangzhou 510632, China*

[3]*School of Environment, Jinan University, Guangzhou 511443, China*

[4]*Institute of Nanophotonics, Jinan University, Guangzhou 511443, China*

[†]These authors contributed equally to this work and should be considered co-first authors

[*]Corresponding authors: Dali WANG and Kai CHEN E-mails: wdali2018@jnu.edu.cn and kaichen@jnu.edu.cn

Abstract: Environmental pollutants, including organic dyes and plastic, have posed severe threats to the health of our ecosystem. Although a lot of efforts have been made to tackle this problem, these pollutants are still massively produced during industrial activities as well as human life. The ability to detect these environmental pollutants with high sensitivity is thus greatly desired. Herein, we propose a novel surface-enhanced Raman spectroscopy (SERS) substrate with high-density hot spots, high Raman signal enhancement, and good uniformity for trace detection of organic pollutants and nanoplastic. The SERS substrates consist of abundant ultranarrow nanogaps that are fabricated with cost-effective colloidal lithography. With the significantly enhanced near-field intensity, rhodamine 6G (R6G) molecules as low as 10^{-8} M can be detected with good linear correlations between the signal intensity and molecular concentrations. Moreover, both nanowells and nanogaps are present on the SERS substrates fabricated by our method and the nanowells could be used to trap micro- or nanoplastic. We successfully demonstrate detecting polystyrene (PS) nanospheres (200 nm in diameter) with different concentrations (1.000% to 0.001%), showing the potential to detect micro- or nanoplastic pollutants in the environment. Our method provides a feasible approach to fabricating low-cost SERS substrates for the detection of organic pollutants and nanoplastic.

Keywords: Nanogap; colloidal lithography; SERS; nanoplastic

Citation: Zhiliang ZHANG, Peibin XU, Hao WU, Churong MA, Jiahao YAN, Tuan GUO, *et al*., "Self-Assembled 10 nm-Nanogap Arrays With High-Density Hot Spot Distribution for Environmental Pollutant Detection," *Photonic Sensors*, 2026, 16(3): 9560021.

1. Introduction

According to the 2018 revision of world urbanization prospects, 55% of the world population was living in cities, and this proportion is expected to increase to 68% by 2050 [1]. With the growth of

Received: 4 August 2025 / Revised: 10 December 2025

DOI: 10.26599/PhoS.2026.9560021
Article type: Research article

the population, environmental pollutants produced directly or indirectly by human beings in industrial production and daily life are also increasing, which could lead to serious risks to the environment and the welfare of people. Nearly 9 million people around the world died due to pollution problems in 2019 [2]. When contaminants are ingested by organisms, severe harm can be done to them, including teratogenic, carcinogenic, and mutagenic effects, as well as endocrine disrupting effects [3–5]. And the transfer of these pollutants through the food chain has seriously threatened human life and health, so environmental problems caused by pollutants have attracted more and more attention. Among various pollutants, organic pollutants and microplastic are widely present in our environment. Generally, organic dyes, such as rhodamine 6G (R6G), are often used in industrial production or food processing [6]. Excessive intake of R6G in humans and animals can cause reproductive, developmental, and chronic toxicity [7]. Besides organic pollutants, a very large amount of plastic waste is generated every year around the world with sizes ranging from bulk to nanoscale [8]. The bulk plastic waste can further break down into small pieces with microscale or nanoscale dimensions, i.e., microplastic or nanoplastic, which can be difficult to detect and thus become a more harmful pollutant source threatening the environment and human health [9–11]. Therefore, methods that can detect trace amounts of organic pollutants and microplastic are highly desirable. While traditional techniques can be used, the instruments are usually bulky, expansive, and complicated for operation. For organic pollutants, liquid chromatography or gas chromatography (GC) is usually used for sampling with high sample requirements and complex detection procedures [12]. And for nanoplastic, detection methods include the pyrolysis gas chromatography-mass spectrometry [13, 14], Fourier transform infrared spectroscopy [13], liquid chromatography-tandem mass spectrometry [15, 16], and Raman spectroscopy [17]. But problems exist with these techniques, such as expensive sample preparation and limited resolution for smaller-sized microplastic.

Surface-enhanced Raman spectroscopy (SERS) has been a powerful analytical technique [18, 19], which can achieve ultrahigh molecular sensitivity thanks to the excitation of plasmon resonances with metallic nanostructures and finds applications in various fields, such as the environmental analysis [20–22]. The SERS has also shown sufficient potential in the detection of organic pollutants and microplastic or nanoplastic [23–27]. Two main factors contribute to the amplification of Raman signals: electromagnetic field enhancement and chemical enhancement. In general, the electromagnetic field enhancement plays a more significant role than chemical enhancement [28]. Therefore, plasmonic nanostructures with very strong near-field intensity (i.e., hot spots) have been extensively studied and applied in various SERS applications [29–33]. Among the reported nanostructures, nanoscale gaps have been one of the most utilized nanostructures because of their ability to confine the field inside nanogaps, leading to enormous near-field enhancement. In addition, the good uniformity, dense distribution of hot spots, and simple fabrication are also very important factors for SERS substrates [34, 35]. While conventional techniques have been used to fabricate SERS substrates, such as the electron beam lithography (EBL) [36, 37] and focused ion beam (FIB) [38], these methods suffer from the high cost and low throughput, which are disadvantageous for practical applications. Alternatively, colloidal lithography (also known as nanosphere lithography) [39, 40], a scalable and versatile nanofabrication technique, is able to generate large-area nanostructures at low cost. Nanostructures, such as nanoholes, nanodisks, nanobowls, and nanocones, have been fabricated using this method [41–47].

In this work, we present a novel SERS substrate featuring abundant highly ordered 10 nm nanogaps and nanowell structures based on colloidal lithography. The fabricated SERS substrates show an excellent detection ability towards organic pollutants (R6G) and nanoplastic [polystyrene (PS) nanospheres]. We experimentally demonstrate that the substrate could detect R6G molecules down to 10^{-8} M with a linear range from 10^{-8} M to 10^{-5} M. Meanwhile, the coexistent nanowell structures help to trap nanoparticles, which is beneficial to the collection of the Raman signals of microplastic or nanoplastic. Nanoplastic with a diameter down to 200 nm is detected at different concentrations.

2. Results and discussion

The nanogap arrays are fabricated with a four-step process based on nanosphere lithography, and the detailed route is illustrated in Fig. 1(a). First, a hexagonal close-packed monolayer of PS nanospheres is prepared on a glass substrate through self-assembly of nanospheres using our previously reported method in [40]. Then, the PS nanosphere monolayer is etched with O_2 plasma to reduce the size of the nanospheres. Afterwards, the etched nanospheres act as masks for metal deposition. A 3 nm Cr layer is deposited on the substrate as the adhesion layer followed by the deposition of a 70 nm gold film. The deposited gold form nanocaps and nanoholes, respectively, on the PS nanospheres and the substrate. Meanwhile, a new structure (nanocavity) is also formed between the nanocap and the nanohole [Fig. 1(c)].

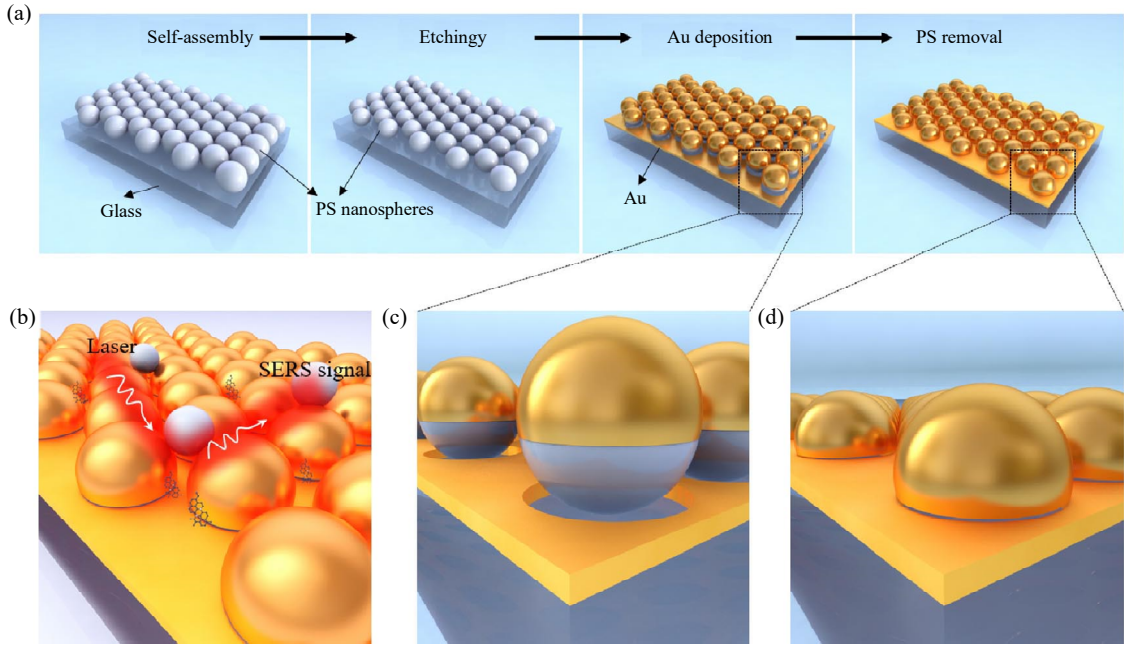

Fig. 1 Fabrication scheme of nanogap arrays: (a) a PS nanosphere monolayer is formed onto the substrate and then etched by O_2 plasma (A gold film is deposited through the PS nanosphere mask. At the last step, the sample is immersed in $CHCl_3$ to remove the spheres.), (b) the schematic diagram of the detection method, and (c) and (d) the enlarged views of the step of Au deposition and the step of dissolving the PS.

The existence of nanocavities can lead to more hot spots and larger electric field enhancement. The field enhancement inside the nanocavity depends greatly on the cavity width. As the final step, the sample is immersed in $CHCl_3$ to completely dissolve the PS spheres, further decreasing the cavity width. As less metal is deposited around the equator area of the spheres, extremely narrow nanocavities (or nanogaps) can be obtained when the nanocaps fall into the nanoholes, as shown in Fig. 1(d). Figure 1(b) shows the sensing scheme of nanoplastic and dye molecules using the nanogap arrays as a SERS

platform. Molecules located near or inside the nanogaps can achieve the higher Raman signal amplification. In addition, the self-assembled structure has another advantage that its geometrical shape facilitates the capture of nanoplastic between the nanocaps, which makes this versatile platform suitable for SERS-active species with varied sizes in different applications.

Figure 2 shows the morphology changes of nanostructures at different fabrication stages. The periodicity of the array is determined by the diameter of the original nanospheres (D=500 nm). At the beginning, the PS nanospheres form highly uniform hexagonal structures [Fig. 2(a)], whose geometrical arrangement is well kept even after O_2 plasma etching.

Figure 2(b) shows the etched PS nanospheres with a diameter of 440 nm, which can be accurately controlled by the etching time. We also fabricate nanosphere monolayers with different periods to achieve different densities of the nanocavity distribution, as shown in Fig. S1, Supplementary files. These PS nanospheres with different diameters are all etched away by 60 nm.

Figure 2(c) shows a cross-section scanning electron microscopy (SEM) image of the sample after gold deposition, where nanocaps are formed over the PS nanospheres while nanoholes are formed on the substrate. Cavities are formed between the nanocaps and the nanoholes with a relatively large cavity width, which is roughly half of the height of a nanosphere. Finally, the samples are heated at 40 ℃ and afterwards the PS nanospheres are dissolved in chloroform, allowing the nanocaps to drop into the corresponding holes. It is noted that the heating process helps to enhance the adhesion of the polystyrene spheres to the substrates, avoiding relative dislocation of the nanocaps and enhancing the repeatability of the fabrication. The samples are then subjected to the O_2 plasma to remove some organic residue on their surfaces (the dark area in Fig. S2, Supplementary files).

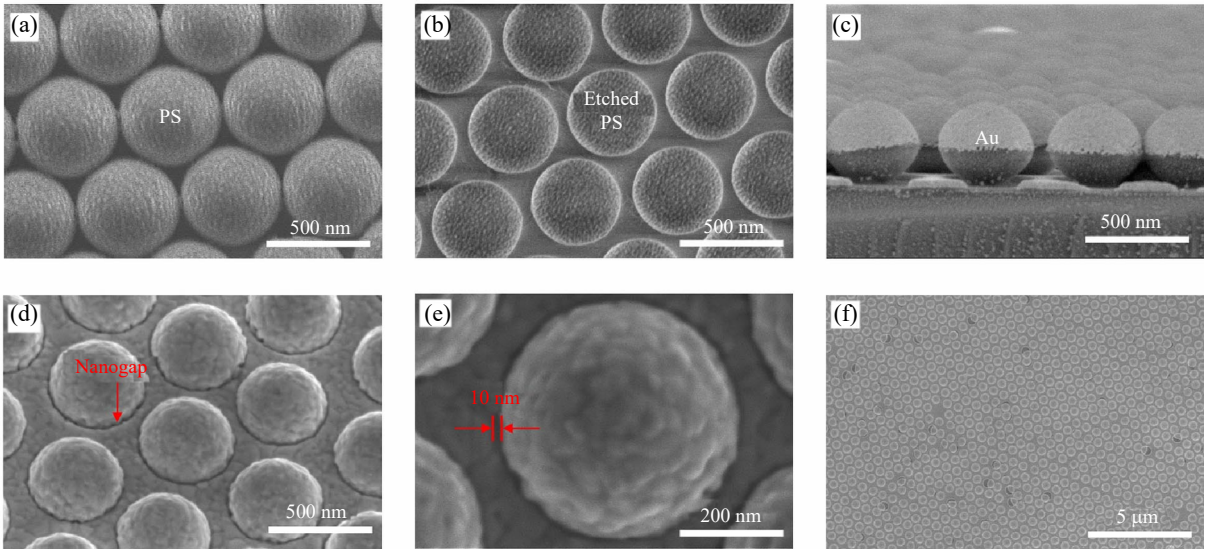

Fig. 2 Morphologies of nanogap arrays at different fabrication stages: (a)–(d) SEM images of the self-assembly step, etching step, Au deposition step, and dissolving the PS step, respectively, (e) the SEM of nanogap arrays with a gap width of 10 nm, and (f) the SEM image of the nanogap array at a large area. Scale bar: (a)–(d) 500 nm, (e) 200 nm, and (f) 5 μm.

Figure 2(d) shows a tilted-view SEM image of the nanogap arrays. The nanogap width varies around the nanocap periphery with values below 10 nm as indicated in Fig. 2(e). Inherited from the good quality of the self-assembled colloidal monolayers, the nanogap arrays show highly uniform distribution over large areas on the scale of centimeters. Figure S3 in Supplementary files,

shows photos of the nanogap arrays fabricated from PS spheres with three different diameters (300 nm, 500 nm, and 1 μm). In addition to SEM imaging, optical transmission measurement is also carried out to monitor the dissolving of PS spheres and the formation of the nanogaps. As shown in Fig. S4, Supplementary files, the transmittance of the sample gradually decreases as the PS nanospheres dissolve. Finally, when the spheres are totally dissolved, the transmittance approaches zero, indicating the formation of the nanogaps as the substrate is now covered with gold except the nanogap region. We also numerically simulate the transmission spectra of the nanogaps, which are in good agreement with the experimental measurement (Fig. S4 in the Supplementary files).

The enhancement of Raman signals largely depends on the enhancement of the electric field, which varies at different wavelengths. In order to achieve better SERS efficiency, the excitation laser of an appropriate wavelength should be selected. We simulate the near field of nanogap arrays under the excitation of three different wavelengths (532 nm, 633 nm, and 785 nm) that are usually used for Raman measurement. We investigate the near-field enhancement spectra of the nanogaps. A point monitor is positioned inside the nanogap as illustrated in the inset of Fig. 3(b). The electric near

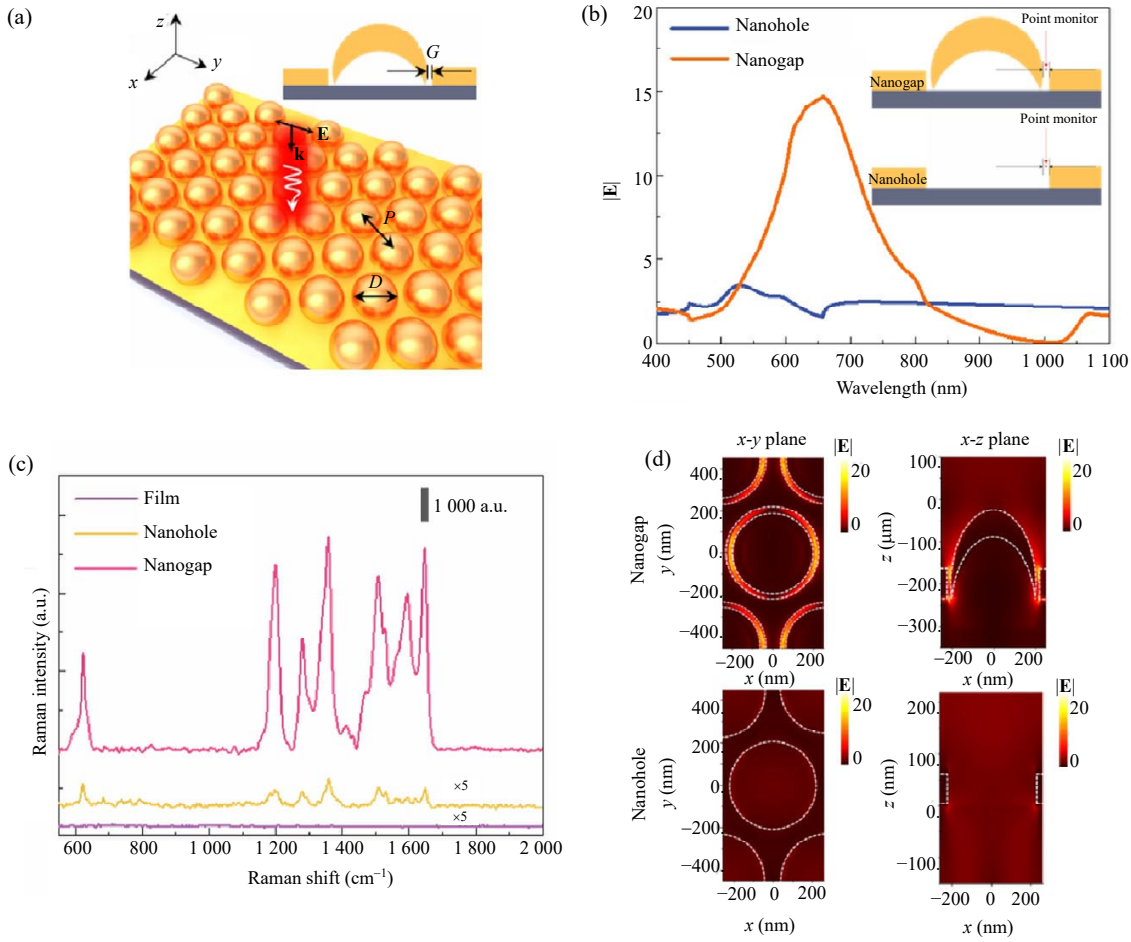

Fig. 3 SERS performance and electromagnetic (EM) field distributions of different structures: (a) illustration of the Au nanogap array [The period (P) and the diameter (D) are 520 nm and 440 nm, respectively and the gap width (G) is 10 nm. **E** and **k** are the polarization and wave vectors of the incident light, respectively], (b) the electric near-field enhancement spectra of the nanogap array and nanohole array (The inset shows the position of the point monitor. It is placed in the middle of the nanogap and at the same distance to the edge for the nanoholes.), (c) the Raman spectra of R6G molecules (10^{-5} M) on film, nanohole arrays, and nanogap arrays, and (d) the EM near-field profile of the nanogap (top) and nanohole array (bottom) at 633 nm (The white dashed lines indicate the nanostructures.).

field is highly enhanced around 650 nm. The electric near-field profile in the *x*-*y* plane is displayed in Fig. S5, Supplementary files, confirming the larger enhancement at 532 nm than that at 633 nm and 785 nm. Therefore, a laser source of 532 nm is used in the subsequent measurement.

SERS performance of the nanogap arrays is evaluated using organic pollutant (R6G, 10^{-5} M) as the probe molecule. We compare the SERS signals of the nanogap array with that of a nanohole array with the same period and hole diameter. As shown in Fig. 3(c), the characteristic Raman peaks from the R6G are clearly shown from the nanogap array, with the signal intensity approximately 36 times larger than that from the nanohole array, while the Au film barely shows any Raman signal. To obtain a better understanding of the intensity difference of the SERS signals, the electric near-field profile of the nanogap and nanohole at 633 nm is obtained and shown in Fig. 3(d). For nanoholes, the field enhancement is low, and the electric field is mainly localized inside the holes. For nanogaps, the near field is concentrated inside the nanogap as well as around the nanocap with much higher field enhancement than that in the nanohole. With more hot spots, it is thus expected that the nanogap arrays can give rise to larger Raman signals, which is consistent with the experiment results shown in Fig. 3(c). Furthermore, as shown in Fig. 3(b), the enhanced near-field magnitude of the nanogaps is ~10 times larger than that of the nanoholes at around 633 nm. The results show the excellent capability of the nanogap arrays for SERS sensing of organic molecules.

In addition to the electric field enhancement, the uniformity of the SERS signals and the density of hot spots are also factors that are key to quantitative SERS measurement and analysis. For the proposed nanogap arrays, since the nanogap width does not depend on the diameter of the PS spheres, we can simply increase the density of the hot spots by using smaller PS nanospheres. To investigate the relationship between the density of hot spots and the SERS performance, we fabricated three nanogap arrays using PS spheres with different diameters. Figures. 4(a)–4(c) show the SEM images of the substrates fabricated with 1 μm, 500 nm, and 300 nm nanospheres, respectively. Simple geometrical calculations reveal that the nanogap area on the sample from 300 nm spheres is 1.2 times and 2.3 times larger than that on the sample from 500 nm and 1 μm spheres, respectively.

We measure the corresponding SERS intensities of the nanogap arrays. On each substrate, we collect the Raman spectra from 5 different spots, and the results are shown in Figs. 4(d)–4(f). All three substrates distinctively show the Raman peaks from the R6G, indicating the good reproducibility of this method. In general, the SERS substrate fabricated from 300 nm PS spheres displays the highest signal intensity, which can be attributed to the increase in the hot spot density. We choose the Raman peak at 1 196 cm^{-1} as the representative signal from the R6G molecules and compare its intensity from these three substrates (Fig. S6, Supplementary files). The peak intensity from the substrate made of 300 nm PS spheres is 1.5 times and 13.2 times higher than those of the substrates with 500 nm and 1 000 nm PS spheres, respectively. In addition, the SERS intensity mapping at 1 196 cm^{-1} over a scanned area (randomly chosen, 5 μm×5 μm) is carried out in order to evaluate the uniformity of the SERS substrates. The step size for the mapping is 625 nm and the results are shown in Figs. 4(g)–4(i), corresponding to the substrates with periods of 1 μm, 500 nm, and 300 nm, respectively. For all these three substrates, the peak intensity shows a few variations across the area, suggesting the good uniformity of the SERS substrates and the excellent reliability of the proposed fabrication method.

In order to investigate the SERS detection ability of the nanogap arrays, R6G solutions with different concentrations are detected by the nanogap arrays with a period of 300 nm. The nanogap substrates are immersed in different R6G aqueous solutions

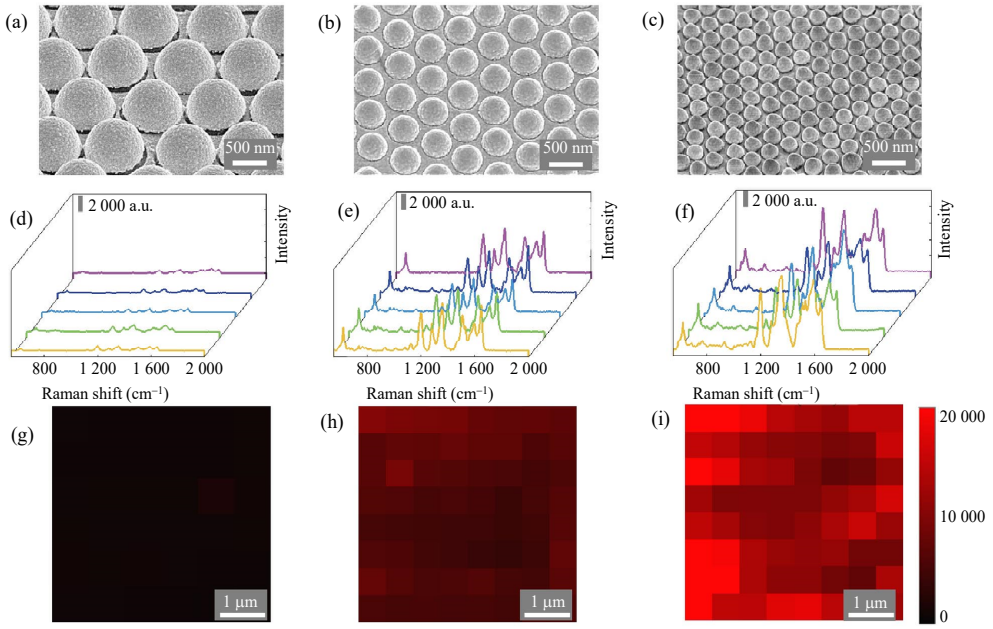

Fig. 4 SERS performance of nanogap arrays fabricated from PS spheres with different diameters, and the SEM images of the nanogap array with (a) 1 μm, (b) 500 nm, and (c) 300 nm PS spheres, the Raman spectra of the sample with (d) 1 μm, (e) 500 nm, and (f) 300 nm PS spheres, and the corresponding Raman mapping in (g)–(i). [The Raman spectra of the 10^{-5} M R6G are collected on 5 random points from each substrate. The SERS intensity mapping images (64×64 pixels) are obtained over a scanned area of 5 μm×5 μm using the 1 196 cm^{-1} Raman peak as the signal.]. Scale bars: (a)–(c) 500 nm and (g)–(i) 1 μm.

(10^{-5} M to 10^{-8} M) for 12 hours, ensuring enough time for the immobilization of R6G molecules onto the substrate surface. As shown in Fig. 5(a), R6G molecules with a concentration as low as 10^{-8} M can be detected, demonstrating the high sensitivity of the nanogap substrate. For concentration calibration, two distinct Raman bands are selected at 623 cm^{-1} and 1 196 cm^{-1}. As shown in Fig. 5(b), there is a good linear relationship between the logarithms of the R6G concentration and logarithms of the Raman intensity at 623 cm^{-1} and 1 196 cm^{-1}, which is very useful for quantitative assays. Therefore, the SERS substrates with the nanogap arrays can be used for molecular detection in various applications because of the high sensitivity and good calibration curve. In the above analysis, the substrates fabricated by the proposed method have proved to be an excellent SERS sensing platform for organic molecules. Besides the abundant nanogaps on the substrate, another advantage of the SERS substrate is the formation of well-shaped nanostructures. As shown in Figs. 1 and 2, nanowells are formed between three adjacent nanocaps. When the aqueous solution of the nanoplastic is dropped onto the substrate, the nanowells can serve as good trapping sites for the plastic nanoparticles when water evaporates, as illustrated in Fig. 5(e), facilitating the occupation of the enhanced near field around the nanocaps and leading to higher SERS signals. For the SERS measurement, PS spheres (200 nm in diameter) are used as model nanoplastic. Figure 5(c) shows the Raman spectra of the PS spheres with various concentrations from 1.000% to 0.001%. The peaks at 619 cm^{-1}, 1 002 cm^{-1}, 1 033 cm^{-1}, and 1 600 cm^{-1} can be attributed to the ring deformation mode, C–C ring breathing mode, CH in-plane deformation band, and C–C stretching vibrations [48, 49]. Clearly, the limit of PS nanosphere detection reaches 0.001%. For the quantitative analysis, a calibrated curve is plotted to show the dependence of the Raman intensity of the typical PS peak at 1 002 cm^{-1} in Fig. 5(d), revealing the linear dependence of the

intensity on the concentration. Figure S7 in Supplementary files, shows the SEM images of various concentrations of PS nanospheres on the SERS platform. Fig. 5(f) shows the SEM of PS nanospheres with the concentration of 0.1% on the SERS substrate. As shown in Fig. 5(g), the enlarged SEM image is the dashed area in Fig. 5(f). The dashed circles are the PS nanospheres with a diameter of 200 nm. As we expected, PS nanospheres are localized into the nanowells. In addition, we also carried out sensing experiments using PS spheres with a diameter of 300 nm. The results are shown in Fig. S8, Supplementary files. It can be seen that the SERS substrates achieve the similar performance that the colloidal concentration as low as 0.001% can be detected for spheres with a diameter of 300 nm, which demonstrates the versatility of the fabricated nanostructures.

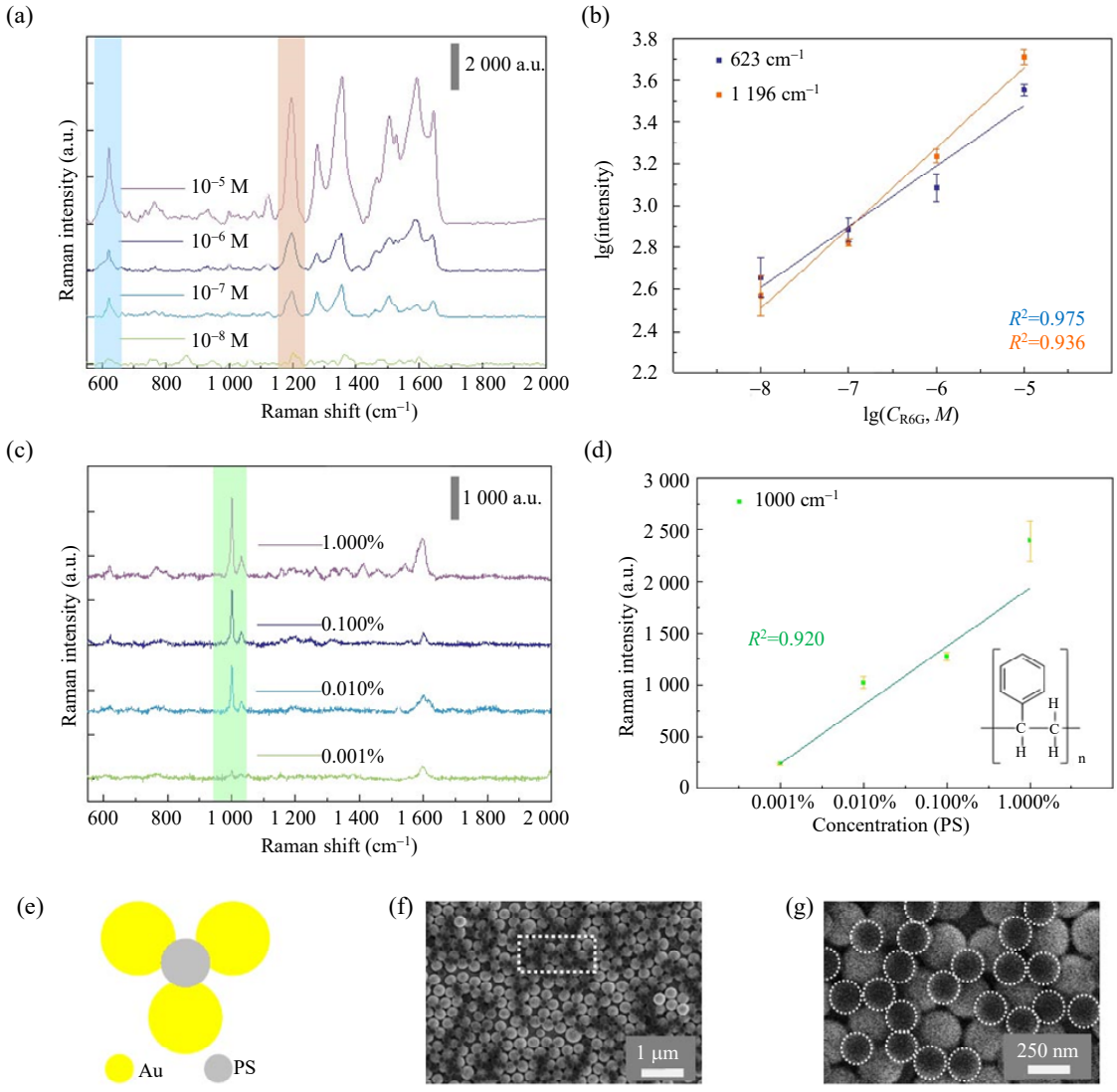

Fig. 5 Nanogap arrays with a period of 300 nm as SERS platforms: (a) SERS spectra of the platform modified with different concentrations of the R6G, (b) the Raman signal intensity of the R6G at 623 cm^{-1} and 1 196 cm^{-1} as a function of the R6G concentration, both axes are in logarithm scale, (c) SERS spectra of the substrate with different concentrations of 200 nm PS nanospheres, (d) the intensity of the Raman peak of PS at 1 002 cm^{-1} as a function of the concentration from 1.000% to 0.001% (The inset shows the molecular structure of polystyrene.), (e) the schematic diagram of trapping the PS nanospheres, (f) the SEM image of PS nanospheres with the concentration of 0.100% on the SERS substrate, and (g) the enlarged SEM image of the dashed area in (f).

3. Conclusions

In conclusion, we have successfully fabricated a highly sensitive SERS substrate with 10 nm-nanogaps and nanowells based on nanosphere lithography. The fabrication method combines nanosphere lithography and selective wet etching to fabricate nanogaps with high-density hot spots. The density can be controlled by varying the periods. The SERS substrate with the period of 300 nm can detect the R6G molecules with a concentration as low as 10^{-8} M. Meanwhile, we show the nanoplastic trapping ability of nanowells using PS nanospheres with a diameter of 200 nm. The fabricated substrates can detect PS nanospheres with concentrations ranging from 1.000% to 0.001%. The nanogap array provides an efficient SERS substrate for the detection of environmental pollutants with varied sizes from organic molecules to the nanoplastic.

4. Experimental section

Nanogap fabrication

Sulfate-functionalized polystyrene spheres with nominal diameters (300 nm, 500 nm, and 1 μm) were purchased from Polyscience Inc., USA and dispersed in a water/ethanol mixture (a 1:1 volume ratio). Glass substrates were cleaned in a mixture of $NH_4OH/H_2O_2/H_2O$ (a 1:1:5 volume ratio) at 80 ℃ for 15 min and blown dry with N_2. The nanospheres formed a close-packed monolayer on the glass substrates by the colloidal lithography method reported previously [40]. The diameter of the PS spheres was reduced by O_2 plasma with isotropic plasma etching: the oxygen flow 10 sccm and radio frequency (RF) power 100 W. The etching time was 7 min for (P=300 nm and D=240 nm), 12 min for (P=500 nm and D=440 nm), and 14 min for (P=1 μm and D=900 nm). A gold film of 70 nm was deposited with the electron beam deposition with 3 nm Cr as the adhesion layer. Then, the sample was heated at 40 ℃ for two minutes before immersed in $CHCl_3$ for 1 hour to remove the etched polystyrene spheres. After that, the surface was dried with the gentle N_2 gas blow. At last, the sample was cleaned by O_2 plasma for 10 min.

Preparation of Raman analyte

R6G was diluted in the de-ionized (DI) water to prepare solutions with different concentrations (10^{-5} M to 10^{-9} M). Then, the SERS substrates were immersed in the prepared solution for 12 hours. After washing with DI water for several times, the substrates were dried with the N_2 gas. For the model nanoplastic, PS nanospheres with a diameter of 200 nm (Baseline, China.) were diluted in DI water to prepare the aqueous solution, ranging from 1% to 0.001%. Then 2 μl of the aqueous solution with various concentrations was dropped onto the SERS substrates and then measured after drying.

Optical and SERS measurement

The morphology of the as-prepared samples was analyzed by a scanning electron microscope (Thermo Fisher Scientific, Czech Republic). Transmission spectra of samples were measured by a fiber-coupled spectrometer (2000PRO, Ocean Optics, USA). The Raman signals were detected using a HORIBA HR Evolution Raman system with a He–Ne 633 nm laser at 15 s exposure time and 2 accumulations under the 10% laser power density. The full power of the 633 nm laser source was 17 mW. Data were collected using a grating of 600 $g{\cdot}mm^{-1}$ and a 50× objective lens with a long working distance. The SERS spectra were collected using the mapping mode under the 50× objective lens.

Numerical simulation

The finite-domain-time-difference (FDTD) method was used to simulate the far-field and near-field properties of the nanogap arrays. In simulations, periodic boundary conditions were used in x and y directions, and the perfectly matched layer (PML) boundary condition was used in the z direction. The refractive index of the glass substrate was fixed at 1.5, and the dielectric constants of Au were taken from Johnson and Christy [50].

Supplementary files

The supplementary files can be downloaded from the webpage of this article in *Photonic Sensors* (https://www.sciopen.com/journal/1674-9251).

Acknowledgment

The authors acknowledge the support from the Guangdong Basic and Applied Basic Research Foundation, China (Grant Nos. 2024A1515010007, 2023B1515020046, 2020A151501905, and 2021A1515012352) and the National Natural Science Foundation of China (Grant Nos. 61975067 and 62005100).

Declarations

Conflict of Interest The authors declare that they have no competing interests.

Use of AI Statement None.

References

[1] United Nations Department of Economic and Social Affairs, World urbanization prospects 2018 revision [Online]. Available, https://population.un.org/wup/publications?tab=2018, 2018.

[2] R. Fuller, P. J. Landrigan, K. Balakrishnan, G. Bathan, S. Bose-O'Reilly, and M. Brauer, "Pollution and health: a progress update," *Lancet Planet Health*, 2022, 6: e535–e547.

[3] Y. Jin, S. Wu, Z. Zeng, and Z. Fu, "Effects of environmental pollutants on gut microbiota," *Environmental Pollution*, 2017, 222: 1–9.

[4] O. M. Alharbi, R. A. Khattab, and I. Ali, "Health and environmental effects of persistent organic pollutants," *Journal of Molecular Liquids*, 2018, 263: 442–453.

[5] A. K. Singh and R. Chandra, "Pollutants released from the pulp paper industry: aquatic toxicity and their health hazards," *Aquatic Toxicology*, 2019, 211: 202–216.

[6] X. Zhao, B. Zhang, K. Ai, G. Zhang, L. Cao, X. Liu, *et al*., "Monitoring catalytic degradation of dye molecules on silver-coated ZnO nanowire arrays by surface-enhanced Raman spectroscopy," *Journal of Materials Chemistry*, 2009, 19(31): 5547–5553.

[7] R. D. Hood, C. L. Jones, and S. Ranganathan, "Comparative developmental toxicity of cationic and neutral rhodamines in mice," *Teratology*, 1989, 40(2): 143–150.

[8] M. MacLeod, H. P. H. Arp, M. B. Tekman, and A. Jahnke, "The global threat from plastic pollution," *Science*, 2021, 373(6550): 61–65.

[9] R. Triebskorn, T. Braunbeck, T. Grummt, L. Hanslik, S. Huppertsberg, M. Jekel, *et al*., "Relevance of nano-and microplastics for freshwater ecosystems: a critical review," *TrAC Trends in Analytical Chemistry*, 2019, 110: 375–392.

[10] R. Geyer, J. R. Jambeck, and K. L. Law, "Production, use, and fate of all plastics ever made," *Science Advances*, 2017, 3(7): e1700782.

[11] A. Ragusa, A. Svelato, C. Santacroce, P. Catalano, V. Notarstefano, O. Carnevali, *et al*., "Plasticenta: first evidence of microplastics in human placenta," *Environment International*, 2021, 146: 106274.

[12] Y. Liu, Z. Lian, F. Li, A. Majid, and J. Wang, "Review on molecular imprinting technology and its application in pre-treatment and detection of marine organic pollutants," *Marine Pollution Bulletin*, 2021, 169: 112541.

[13] E. Hendrickson, E. C. Minor, and K. Schreiner, "Microplastic abundance and composition in western Lake Superior as determined via microscopy, Pyr-GC/MS, and FTIR," *Environmental Science & Technology*, 2018, 52(4): 1787–1796.

[14] F. Saliu, S. Montano, B. W. Hoeksema, M. Lasagni, and P. Galli, "A non-lethal SPME-LC/MS method for the analysis of plastic-associated contaminants in coral reef invertebrates," *Analytical Methods*, 2020, 14: 1935–1942.

[15] L. Wang, J. Zhang, S. Hou, and H. Sun, "A simple method for quantifying polycarbonate and polyethylene terephthalate microplastics in environmental samples by liquid chromatography – tandem mass spectrometry," *Environmental Science & Technology Letters*, 2017, 4: 530–34.

[16] A. Kunz, B. A. Walther, L. Löwemark, and Y. C. Lee, "Distribution and quantity of microplastic on sandy beaches along the northern coast of Taiwan," *Marine Pollution Bulletin*, 2016, 111(1–2): 126–135.

[17] C. F. Araujo, M. M. Nolasco, A. M. Ribeiro, and P. J. Ribeiro-Claro, "Identification of microplastics using Raman spectroscopy: latest developments and future prospects," *Water Research*, 2018, 142: 426–440.

[18] X. X. Han, R. S. Rodriguez, C. L. Haynes, Y. Ozaki,

and B. Zhao, "Surface-enhanced Raman spectroscopy," *Nature Reviews Methods Primers*, 2022, 1: 87.

[19] J. Yi, E. M. You, R. Hu, D. Y. Wu, G. K. Liu, Z. L. Yang, *et al*., "Surface-enhanced Raman spectroscopy: a half-century historical perspective," *Chemical Society Reviews*, 2025, 54: 1453–1551.

[20] E. C. Lin, J. Fang, S. C. Park, F. W. Johnson, and H. O. Jacobs, "Effective localized collection and identification of airborne species through electrodynamic precipitation and SERS-based detection," *Nature Communications*, 2013, 4: 1636.

[21] L. Lv, L. He, S. Jiang, J. Chen, C. Zhou, J. Qu, *et al*., "In situ surface-enhanced Raman spectroscopy for detecting microplastics and nanoplastics in aquatic environments," *Science of The Total Environment*, 2020, 728: 138449.

[22] Q. T. Lê, N. H. Ly, M. K Kim, S. H. Lim, S. J. Son, K. D. Zoh, *et al*., "Nanostructured Raman substrates for the sensitive detection of submicrometer-sized plastic pollutants in water," *Journal of Hazardous Materials*, 2021, 402: 123499.

[23] L. Zhang, Y. Guo, R. Hao, Y. Shi, H. You, H. Nan, *et al*., "Ultra-rapid and highly efficient enrichment of organic pollutants via magnetic mesoporous nanosponge for ultrasensitive nanosensors," *Nature Communications*, 2021, 12: 6849.

[24] L. Zhang, R. Zhao, Y. Wu, Z. Zhang, Y. Chen, M. Liu, *et al*., "Ultralow-background SERS substrates for reliable identification of organic pollutants and degradation intermediates," *Journal of Hazardous Materials*, 2023, 460: 132508.

[25] O. Guselnikova, A. Trelin, Y. Kang, P. Postnikov, M. Kobashi, A. Suzuki, *et al*., "Pretreatment-free SERS sensing of microplastics using a self-attention-based neural network on hierarchically porous Ag foams," *Nature Communications*, 2024, 15: 4351.

[26] A. Wang, Q. Ding, J. Mou, H. Qi, J. Yang, U. K. Makhmanov, *et al*., "Breaking the size barrier: SERS-Based ultrasensitive detection and quantification of polystyrene plastics in real water samples," *Analytical Chemistry*, 2025, 97: 24340–24349.

[27] W. Lu, J. Luo, Y. Zhuang, J. Liang, M. Xiong, H. Liu, *et al*., "Plasmon enhanced universal SERS detection of hierarchical plastics by 3D plasmonic funnel metastructure," *Advanced Science*, 2025, 12(23): 2500062.

[28] A. Minopoli, A. Acunzo, B. D. Ventura, and R. Velotta, "Nanostructured surfaces as plasmonic biosensors: a review," *Advanced Materials Interfaces*, 2022, 9(2): 2101133.

[29] K. N. Kanipe, P. P. Chidester, G. D. Stucky, and M. Moskovits, "Large format surface-enhanced Raman spectroscopy substrate optimized for enhancement and uniformity," *ACS Nano*, 2016, 10(8): 7566–7571.

[30] D. Lin, Z. Wu, S. Li, W. Zhao, C. Ma, J. Wang, *et al*., "Large-area Au-nanoparticle-functionalized Si nanorod arrays for spatially uniform surface-enhanced Raman spectroscopy," *ACS Nano*, 2017, 11(2): 1478–1487.

[31] A. Zhu, X. Zhao, M. Cheng, L. Chen, Y. Wang, X. Zhang, *et al*., "Nanohoneycomb surface-enhanced Raman spectroscopy-active chip for the determination of biomarkers of hepatocellular carcinoma," *ACS Applied Materials & Interfaces*, 2019, 11(47): 44617–44623.

[32] R. Rastogi, H. Arianfard, D. Moss, S. Juodkazis, P. M. Adam, and S. Krishnamoorthy, "Analyte co-localization at electromagnetic gap hot-spots for highly sensitive (bio)molecular detection by plasmon enhanced spectroscopies," *ACS Applied Materials & Interfaces*, 2021, 13: 9113–9121.

[33] Q. Zhao, H. Yang, B. Nie, Y. Luo, J. Shao, and G. Li, "Wafer-scale and cost-effective manufacturing of controllable nanogap arrays for highly sensitive SERS sensing," *ACS Applied Materials & Interfaces*, 2022, 14: 3580–3590.

[34] M. Moskovits, "Persistent misconceptions regarding SERS," *Physical Chemistry Chemical Physics*, 2013, 15: 5301–5311.

[35] G. Braun, S. J. Lee, M. Dante, T. Q. Nguyen, M. Moskovits, and N. Reich, "Surface-enhanced Raman spectroscopy for DNA detection by nanoparticle assembly onto smooth metal films," *Journal of the American Chemical Society*, 2007, 129(20): 6378–6379.

[36] R. Regmi, J. Berthelot, P. M. Winkler, M. Mivelle, J. Proust, F. Bedu, *et al*., "All-dielectric silicon nanogap antennas to enhance the fluorescence of single molecules," *Nano Letters*, 2016, 16(8): 5143–5151.

[37] H. Duan, H. Hu, K. Kumar, Z. Shen, and J. K. Yang, "Direct and reliable patterning of plasmonic nanostructures with sub-10-nm gaps," *ACS Nano*, 2011, 5(9): 7593–7600.

[38] M. Melli, A. Polyakov, D. Gargas, C. Huynh, L. Scipioni, W. Bao, *et al*., "Reaching the theoretical resonance quality factor limit in coaxial plasmonic nanoresonators fabricated by Helium ion lithography," *Nano Letters*, 2013, 13(6): 2687–2691.

[39] Z. Chen, C. Y. Jao, K. Hu, Y. Luo, C. Ma, R. Jiang, *et al*., "Plasmonic hybrid modes in a multifunctional ZIF-8 layer for high performance volatile organic compounds sensing," *Optics & Laser Technology*, 2024, 176: 110967.

[40] Z. Zhang, F. Zhao, R. Gao, C. Y. Jao, C. Ma, J. Li, *et al*., "Rayleigh anomaly-enabled mode hybridization in gold nanohole arrays by scalable colloidal lithography for highly-sensitive biosensing," *Nanophotonics*, 2022, 11(3): 507–517.

[41] B. Ai, Y. Yu, H. Möhwald, L. Wang, and G. Zhang, "Resonant optical transmission through

topologically continuous films," *ACS Nano*, 2014, 8(2): 1566–1575.

[42] P. Moitra, B. A. Slovick, W. Li, I. I. Kravchencko, D. P. Briggs, S. Krishnamurthy, *et al*., "Large-scale all-dielectric metamaterial perfect reflectors," *ACS Photonics*, 2015, 2(6): 692–698.

[43] Y. Li, X. Ye, Y. Ma, and L. Qi, "Interfacial nanosphere lithography toward Ag_2S-Ag heterostructured nanobowl arrays with effective resistance switching and enhanced photoresponses," *Small*, 2015, 11(9–10): 1183–1188.

[44] X. Fang, C. Zheng, Z. Yin, Z. Wang, J. Wang, J. Liu, *et al*., "Hierarchically ordered silicon metastructures from improved self-assembly-based nanosphere lithography," *ACS Applied Materials & Interfaces*, 2020, 12(10): 12345–12352.

[45] Z. Wang, J. Liu, X. Fang, J. Wang, Z. Yin, H. He, *et al*., "Plasmonically enhanced photoluminescence of monolayer MoS_2 via nanosphere lithography-templated gold metasurfaces," *Nanophotonics*, 2021, 10(6): 1733–1740.

[46] F. Xu, Z. Zhang, J. Ma, C. Ma, B. O. Guan, and K. Chen, "Large-area ordered palladium nanostructures by colloidal lithography for hydrogen sensing," *Molecules*, 2022, 27(18): 6100.

[47] K. Chen, T. D. Dao, T. D. Ngo, H. D. Ngo, A. Tamanai, S. Ishii, *et al*., "Enhanced photocurrent generation from indium-tin-oxide/Fe_2TiO_5 hybrid nanocone arrays," *Nano Energy*, 2020, 76: 104965.

[48] J. R. Anema, A. G. Brolo, A. Felten, and C. Bittencourt, "Surface-enhanced Raman scattering from polystyrene on gold clusters," *Journal of Raman Spectroscopy*, 2010, 41(7): 745–751.

[49] L. Chang, S. Jiang, J. Luo, J. Zhang, X. Liu, C. Y. Lee, *et al*., "Nanowell-enhanced Raman spectroscopy enables the visualization and quantification of nanoplastics in the environment," *Environmental Science: Nano*, 2022, 9(2): 542–553.

[50] P. B. Johnson and R. W. Christy, "Optical constants of the noble metals," *Physical Review B*, 1972, 6: 4370–4379.